Supplementary information for the letter: "Gravitational Waves from Binary Black Hole Mergers Inside of Stars"

Joseph M. Fedrow,[1,*] Christian D. Ott,[1,2] Ulrich Sperhake,[3,2]
Jonathan Blackman,[2] Roland Haas,[4] Christian Reisswig,[2] and Antonio De Felice[1]

[1] *Center for Gravitational Physics and International Research Unit of Advanced Future Studies, Yukawa Institute for Theoretical Physics, Kyoto University, Kyoto, Japan*
[2] *TAPIR, Walter Burke Institute for Theoretical Physics, California Institute of Technology, Pasadena, CA, USA*
[3] *Department of Applied Mathematics and Theoretical Physics, Centre for Mathematical Sciences, University of Cambridge, Cambridge, United Kingdom*
[4] *National Center for Supercomputing Applications, University of Illinois at Urbana-Champaign, 1205 W Clark St, Urbana, IL 61801, USA*

(Dated: August 25, 2017)

PACS numbers: 04.25.D-, 04.25.dg, 04.30.Db

ANALYSIS DETAILS

Gravitational Wave Mismatch Calculation. The mismatch between two observed waveforms $h^1(t)$ and $h^2(t)$ is defined as one minus the maximum overlap $\mathcal{O}(h^1, h^2)$,

$$\mathcal{M}(h^1, h^2) = 1 - \max_{\{\chi_i\}} \mathcal{O}(h^1, h^2)\,, \tag{1}$$

where the overlap is given by

$$\mathcal{O}(h^1, h^2) = \frac{\langle h^1|h^2\rangle}{\sqrt{\langle h^1|h^1\rangle\langle h^2|h^2\rangle}}\,. \tag{2}$$

Here, $\langle\cdot|\cdot\rangle$ is a detector-noise weighted inner product and optimization is carried out over a set $\{\chi_i\}$ of parameters impacting the overlap (e.g., shifts in waveform phases, polarization angles, arrival times) [1].

In the simplest case, we can choose $\langle\cdot|\cdot\rangle$ as the frequency-domain noise weighted inner product [2],

$$\langle a|b\rangle_f = 4\mathrm{Re}\int_0^\infty \frac{\tilde{a}(f)\tilde{b}^*(f)}{S_n(f)}df\,. \tag{3}$$

Here, $S_n(f)$ is the detector noise power spectral density and $\tilde{a}(f)$ is the Fourier transform of $a(t)$.

The real gravitational wave signal $h(t)$ observed by a single detector is given by

$$h(t) = F_+ h_+ + F_\times h_\times\,, \tag{4}$$

where F_+ and $F_\times$ are the detector antenna pattern functions that depend on the sky location of the source and polarization basis (see, e.g., [3]).

We now consider two scenarios: (1) A best case in which both h_+ and $h_\times$ are measured by two optimally oriented GW detectors at Advanced LIGO design sensitivity ("ZDHP" for zero-detuning, high-power [4]). (2) The realistic scenario of the two Advanced LIGO interferometers with the sensitivity at the time of GW150914.

For both cases, we need the two-detector inner product for two detectors α and β, which is defined [3] as the sum of the single-detector contributions,

$$\langle h^1|h^2\rangle_{\rm 2det} = \langle h^{1,\alpha}|h^{2,\alpha}\rangle_s + \langle h^{1,\beta}|h^{2,\beta}\rangle_s\,. \tag{5}$$

Here, $h^{1,\alpha}$ is waveform 1 as seen by detector α through Eq. 4 and so forth. The single-detector inner product $\langle\cdot,\cdot\rangle_s$ used is that given by Eq. 3 with the exception that we integrate over some frequency interval defined by $[f_{\rm min}, f_{\rm max}]$. In practice, we obtain the necessary Fourier transforms by using the Fast Fourier Transform algorithm after tapering the ends of the time domain signal and padding with zeros for all waveforms to have the same length in the time domain.

For scenario (1), we follow [5] and define an optimal two-detector $\mathcal{O}_{\rm opt}$ overlap by choosing detectors oriented so that one detector is maximally sensitive to h_+ (and insensitive to $h_\times$) while the opposite is true for the other detector. We then have

$$\langle h^1|h^2\rangle_{\rm opt} = \langle h^1_+|h^2_+\rangle_s + \langle h^1_\times|h^2_\times\rangle_s\,, \tag{6}$$

with $S_n(|f|)$ in Eq. 3 chosen as the Advanced LIGO ZDHP noise power spectral density. $\mathcal{O}_{\rm opt}$ is then given by Eq. 2 with $\langle\cdot|\cdot\rangle_{\rm opt}$ and the mismatch is obtained as $\mathcal{M}_{\rm ZDHP} = 1 - \max\mathcal{O}_{\rm opt}$. We optimize over time shifts and polarization angle shifts of the waveforms. Since we consider only the $(2,2)$ GW mode, we simply assume a face-on direction of GW propagation, and orbital phase shifts are identical to polarization phase shifts. See [5] for further details.

For scenario (2), we use the inner product of Eq. 5 with the Advanced LIGO Hanford and Livingston antenna patterns [6] for GW150914 and the parameters given in [7]. We employ the actual Hanford and Livingston noise power spectral densities at the time of GW150914 provided at `https://losc.ligo.org/events/GW150914/`. We obtain $\mathcal{M}_{\rm GW150914} = 1 - \max\mathcal{O}_{\rm GW150914}$ for the

(2, 2) GW mode by optimizing over time shifts, polarization angle shifts, and orbital phase shifts. We neglect contributions from other GW modes.

Reduction in Log-Likelihood due to Mismatch. In GW parameter estimation, the posterior probability of a BBH parameter vector $\vec{\vartheta}$ is determined from the prior and likelihood. The GW likelihood function (e.g., [8]) is given by

$$\mathcal{L}(d|\vec{\vartheta}) \propto \exp\left[-\frac{1}{2}\left\langle h^{\rm M}(\vec{\vartheta}) - d|h^{\rm M}(\vec{\vartheta}) - d\right\rangle\right] . \quad (7)$$

Here, $d = h^{\rm GR} + n$ is the data observed in the detectors consisting of the GR signal (we use "GR" as a synonym for "true") and detector noise n. $h^{\rm M}$ is the template waveform generated by some waveform model.

The log-likelihood is then

$$\log\mathcal{L} = {\rm C} - \left[\frac{1}{2}\langle h^{\rm M}|h^{\rm M}\rangle + \frac{1}{2}\langle h^{\rm GR}|h^{\rm GR}\rangle + \frac{1}{2}\langle n|n\rangle - \langle n|h^{\rm M} - h^{\rm GR}\rangle - \langle h^{\rm M}|h^{\rm GR}\rangle\right] , \quad (8)$$

where C is a constant of proportionality.

Suppose that $h^{\rm M}$ is different from the true signal,

$$h^{\rm M} = (1+\epsilon_1)h^{\rm GR} + \epsilon_2 h^{\perp} , \quad (9)$$

where $\langle h^{\perp}|h^{\rm GR}\rangle = 0$. Here ϵ_1 and ϵ_2 are numbers and we consider the limit $\epsilon_{1,2} \ll 1$. Any $h^{\rm M}$ can be decomposed in this way. The log-likelihood becomes

$$\log\mathcal{L} = \log\mathcal{L}_0 - \frac{1}{2}\epsilon_1^2\langle h^{\rm GR}|h^{\rm GR}\rangle - \frac{1}{2}\epsilon_2^2\langle h^{\perp}|h^{\perp}\rangle + \epsilon_1\langle n|h^{\rm GR}\rangle + \epsilon_2\langle n|h^{\perp}\rangle , \quad (10)$$

where $\log\mathcal{L}_0$ is the log-likelihood when $h^M = h^{\rm GR}$. The expected reduction in the log-likelihood is then

$$\mathrm{E}[\delta\log\mathcal{L}] = \frac{1}{2}\epsilon_1^2\langle h^{\rm GR}|h^{\rm GR}\rangle + \frac{1}{2}\epsilon_2^2\langle h^{\perp}|h^{\perp}\rangle . \quad (11)$$

We now allow a small bias in the distance to the source by rescaling $h^{\rm M}$ by $(1+\epsilon_1)^{-1}$ with which we obtain the convenient expression

$$\mathrm{E}[\delta\log\mathcal{L}] = \frac{1}{2}\epsilon_2^2\langle h^{\perp}|h^{\perp}\rangle + \mathcal{O}(\epsilon^3) . \quad (12)$$

The mismatch between $h^{\rm GR}$ and $h^{\rm M}$ is

$$\mathcal{M}(h^{\rm GR}, h^{\rm M}) = 1 - \frac{\langle h^{\rm GR}|h^{\rm M}\rangle}{\sqrt{\langle h^{\rm GR}|h^{\rm GR}\rangle\langle h^{\rm M}|h^{\rm M}\rangle}} \quad (13)$$

$$= \frac{1}{2}\epsilon_2\frac{\langle h^{\perp}|h^{\perp}\rangle}{\langle h^{\rm GR}|h^{\rm GR}\rangle} + \mathcal{O}(\epsilon^3) , \quad (14)$$

where optimization over phase shifts, time shifts, etc. is implicit.

The signal-to-noise ratio ϱ is given by $\varrho^2 = \langle h^{\rm GR}|h^{\rm GR}\rangle$. With this, we find

$$\mathrm{E}[\delta\log\mathcal{L}] \approx \varrho^2\mathcal{M} . \quad (15)$$

The posterior probability will be affected by a factor of Euler's number e when $\delta\log\mathcal{L} = 1$, which can be considered a mild observational inconsistency. Hence, the mismatch $\mathcal{M}$ will begin to have an effect on GW data analysis when

$$\mathcal{M} \gtrsim \frac{1}{\varrho^2} . \quad (16)$$

NUMERICAL CONVERGENCE

We carry out additional simulations at coarse-grid resolutions $\Delta x_1 = 1.00\,M$ and $\Delta x_3 = 1.60\,M$, in addition to our standard-resolution simulations of $\Delta x_2 = 1.25\,M$. For our convergence analysis, we choose the vacuum (G0) and the highest density (G4) as two extremes of the simulations we carry out. We focus our analysis on the gravitational waveforms since these are the most important output of our simulations.

In Fig. 1, we show numerical convergence in the Newman-Penrose scalar ψ_4 between the different resolutions for the G0 vacuum simulation. We consider phase and amplitude differences separately. The amplitude is defined as

$$A(t) = \sqrt{{\rm Re}[\psi_4(t)]^2 + {\rm Im}[\psi_4(t)]^2} , \quad (17)$$

while the phase is defined as

$$\phi(t) = \tan^{-1}\left(\frac{{\rm Im}[\psi_4(t)]}{{\rm Re}[\psi_4(t)]}\right) , \quad (18)$$

where ${\rm Re}[\psi_4]$ and ${\rm Im}[\psi_4]$ are the real and imaginary parts of ψ_4, respectively. Our numerical scheme is fourth-order, hence, we expect fourth-order convergence and a self-convergence factor of

$$Q_s = \frac{\Delta x_3^n - \Delta x_2^n}{\Delta x_2^n - \Delta x_1^n} = 0.3505 , \quad (19)$$

where n is the order of convergence. In Fig. 1, we rescale the differences between highest resolution and second-highest (i.e. standard) resolution by $1/Q_s$. These rescaled curves lie essentially on top of the curves for the differences between second-highest and lowest resolution, demonstrating approximate fourth-order convergence.

In Fig. 2 we perform the same analysis for the highest-density simulation G4. In this case, the hydrodynamics plays an important role in driving the coalescence. If our finite-volume implementation dominates the numerical error, we expect second-order convergence when the flow is smooth. However, soon after the start of the simulation, steep density gradients and shocks develop for which

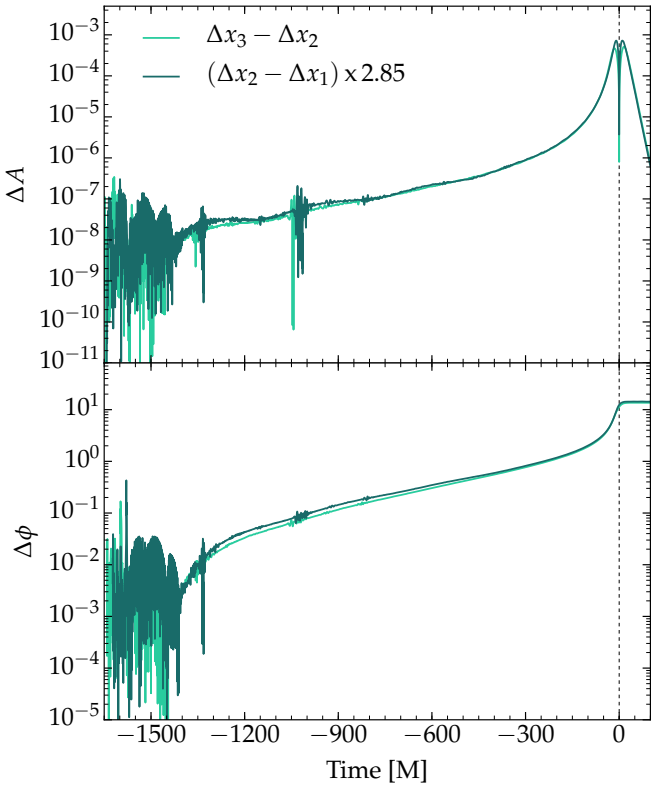

FIG. 1: Fourth-order convergence for the G0 vacuum simulation. The dashed line at $0\,M$ corresponds to merger, which we define as the maximum of the h_{22} amplitude, and the time is given relative to merger. *Top:* Amplitude differences between our lowest (Δx_3), standard (Δx_2), and highest-resolution (Δx_1) simulations. We scale the differences using the self-convergence factor $1/Q_s = 2.85$ corresponding to fourth-order convergence for this choice of resolutions. *Bottom:* Phase angle differences also exhibiting fourth-order convergence.

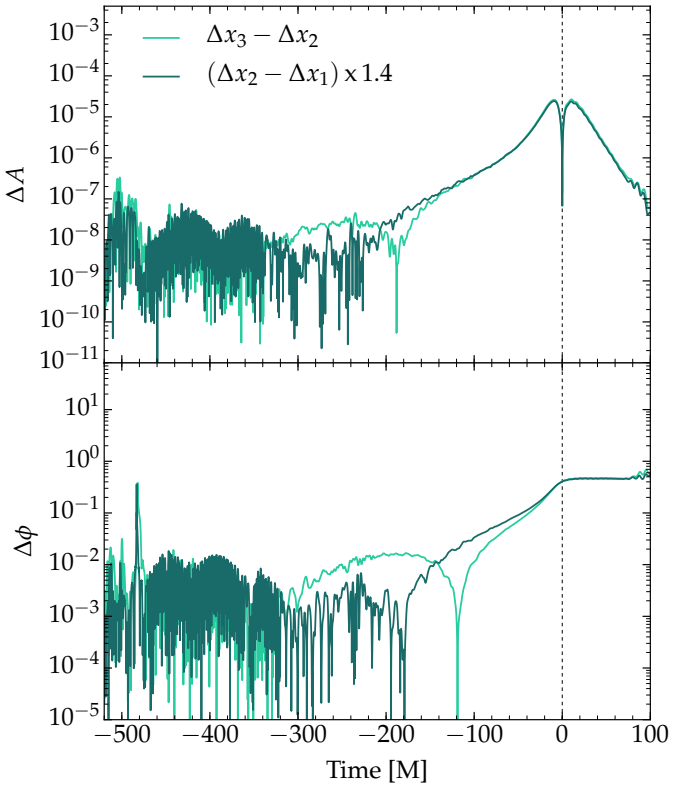

FIG. 2: Convergence of the G4 simulation. The waveforms are aligned at merger, as defined in Figure 1, and all times are given relative to merger. The merger time is $0\,M$, marked with a dashed vertical line. *Top:* Difference in waveform amplitude. We scale the difference between Δx_2 and Δx_1 by a self-convergence factor of $1/Q_s = 1.4$, corresponding to first-order convergence. These are the simulations with the highest gas density and the evolution shows steep density gradients and shocks. Hence, we expect first-order convergence. *Bottom:* Phase angle differences between the different resolution pairs, also exhibiting approximate first-order convergence.

our numerical scheme (as any high-resolution shock capturing scheme) is only first-order convergent. Hence, we can only expect first-order convergence. We compute a first-order self-convergence factor $Q_s = 0.7143$, with $1/Q_s = 2.85$. Figure 2 shows that we obtain roughly first-order convergence in GW amplitude and phase.

In order to clarify how numerical resolution effects the main results of our paper, we have calculate mismatches between various resolutions for the G0 and G4 cases. For the G0 case we find the mismatches to be 1.6×10^{-3} between high and medium resolution, 2.9×10^{-3} between medium and low resolution, and 3.5×10^{-3} between high and low resolution. For the G4 case the mismatches are 3.5×10^{-5} between high and medium resolution, 1.0×10^{-4} between medium and low resolution, and 2.3×10^{-4} between high and low resolution. Comparing these results with the mismatches listed in Table 1 (in the main paper), we conclude that our main conclusions are independent of numerical resolution.

* Electronic address: jfedrow@yukawa.kyoto-u.ac.jp

[1] T. Damour, B. R. Iyer, and B. S. Sathyaprakash, Phys. Rev. D. **57**, 885 (1998).
[2] C. Cutler and É. E. Flanagan, Phys. Rev. D. **49**, 2658 (1994).
[3] I. W. Harry and S. Fairhurst, Phys. Rev. D. **83**, 084002 (2011).
[4] D. Shoemaker, Tech. Rep. LIGO-T0900288-v3, LIGO Scientific Collaboration (2010), URL https://dcc.ligo.org/LIGO-T0900288/public.
[5] J. Blackman, S. E. Field, M. A. Scheel, C. R. Galley, D. A. Hemberger, P. Schmidt, and R. Smith, Phys. Rev. D. **95**, 104023 (2017).
[6] W. Althous, L. Jones, and A. Lazzarini, Tech. Rep. LIGO-T980044-10, LIGO Laboratory (1997), URL https://dcc.ligo.org/T980044/public.
[7] B. P. Abbott, R. Abbott, T. D. Abbott, M. R. Abernathy, F. Acernese, K. Ackley, C. Adams, T. Adams, P. Addesso,

R. X. Adhikari, et al., Class. Quantum Grav. **34**, 104002 (2017).
[8] B. P. Abbott, R. Abbott, T. D. Abbott, M. R. Abernathy, F. Acernese, K. Ackley, C. Adams, T. Adams, P. Addesso, R. X. Adhikari, et al., Phys. Rev. Lett. **116**, 241102 (2016).